Ore Geology Reviews 157 (2023) 105409

Contents lists available at ScienceDirect

Ore Geology Reviews

journal homepage: www.elsevier.com/locate/oregeorev

Modes of occurrence of lithium in black shale in the Nandan area, Guangxi, SW China: Implications for clay-type resources

Haonan Zhao [a], Kunyue Ling [a,*], Shunqiao Qin [b], Meirong Lei [b], Hanjie Wen [c,d,*]

[a] State Key Laboratory of Ore Deposit Geochemistry, Institute of Geochemistry, Chinese Academy of Sciences, Guiyang 550081, China
[b] The Seventh Geological Team of Guangxi Zhuang Autonomous Region, Liuzhou 545100, China
[c] School of Earth Science and Resources, Chang'an University, Xi'an 710054, China
[d] College of Earth and Planetary Sciences, University of Chinese Academy of Sciences, Beijing 100049, China

ARTICLE INFO

Keywords:
Lithium resource
Black shale
Li occurrence
Illite

ABSTRACT

Lithium is used in rechargeable batteries due to its high electrochemical potential, and the rapid development of electric vehicles is exerting increasing pressure on reserves. Currently, pegmatites and brine deposits are the two main Li sources, although volcanic clay-type and carbonate-hosted clay-type that formed mainly in continental or coastal basins are receiving increasing attention due to their large size and potential as future Li sources. However, mechanisms of clay Li enrichment are still debated. Marine black shale at the top of the upper Carboniferous-lower Permian Maping Formation in the Nandan area, northern Guangxi, SW China, is enriched in Li to levels of ~1000 ppm. Knowledge of its genetic mechanism would contribute to understanding the geochemical behaviour and enrichment mechanisms of Li in surface environments. The different geological features of the shale, relative to the above clay types, suggest that the Nandan shale is a new type of Li-rich sedimentary rock. Its whole-rock Li contents are positively correlated with K_2O and illite contents, indicating that illite ($K_{0.7}Al_2[(Si,Al)_4O_{10}](OH)_2$) is the carrier of Li in the shale, as supported by high shale Al, Si, K, and Li contents in the *in situ* images. Mineralogical studies have revealed that the Li-rich illite is of detrital origin and was formed during continental weathering. The widespread occurrence of framboidal pyrite and high contents of TOC in the shale indicate that Li-rich shales formed under anoxic depositional conditions. Our findings may provide reference material for the study of the genesis of clay-type Li resources.

1. Introduction

Lithium and its compounds are used in rechargeable batteries (65% of total Li usage globally), ceramics and glass (18%), lubricating greases (5%), polymer production (3%), air conditioners and elsewhere (Bowell et al., 2020). The consumption of Li is increasing exponentially due to the demand for Li-ion batteries for electric vehicles, computers and phones (Bradley et al., 2017).

Lithium is obtained from a variety of natural sources (Meshram et al., 2014; Rosales et al., 2019), with global reserves being of three main types (Bowell et al., 2020; Wen et al., 2020; Ling et al., 2021; Cui et al., 2022): (1) pegmatite deposits with Li mineralisation (e.g., lepidolite and spodumene) in igneous rocks formed during late-stage crystallisation of silicic magmas, and related to granitic pegmatites, highly peralkaline rocks and metasomatic rocks associated with pegmatites; (2) brine deposits formed from Li-rich solutions in both underground and surficial environments; and (3) volcanic clay-type deposits where Li is structurally bound in clays such as hectorite [$Na_{0.3}(Mg,Li)_3Si_4O_{10}(OH)_2$] and jadarite [$LiNaB_3SiO_7(OH)$], and with Li being derived by the dissolution and leaching of adjacent Li-rich volcanic materials. Clay-type deposits are receiving increasing attention due to their large size and potential as Li sources (Meshram et al., 2014; Castor and Henry, 2020). The McDermitt/Kings Valley region, Nevada, USA (e.g., Glanzman et al., 1978; Kesler et al., 2012) and the Jadar region, Serbia (Stanley et al., 2007; Rio Tinto, 2017, Stojadinovic et al., 2017) are potential world-class deposits.

In China, abundant Li-rich sedimentary rocks (clays or bauxitic clay with Li > 0.05 wt%) occur in Guangxi, Guizhou, Yunnan, Henan and Shanxi provinces with Li contents of up to 1.7 wt% (Shen et al., 1986; Song et al., 1987; Chen and Chai, 1997; Wang et al., 2012; Wang et al., 2013; Yu et al., 2016; Cui et al., 2019; Yang et al., 2019a; Yang et al., 2019b; Ling et al., 2020, 2021; Cui et al., 2022; Zhang et al., 2022). Such

* Corresponding authors at: School of Earth Science and Resources, Chang'an University, Xi'an 710054, China (H. Wan).
E-mail addresses: lingkunyue@mail.gyig.ac.cn (K. Ling), wenhanjie@vip.gyig.ac.cn (H. Wen).

https://doi.org/10.1016/j.oregeorev.2023.105409
Received 5 January 2023; Received in revised form 12 March 2023; Accepted 21 March 2023
Available online 24 March 2023

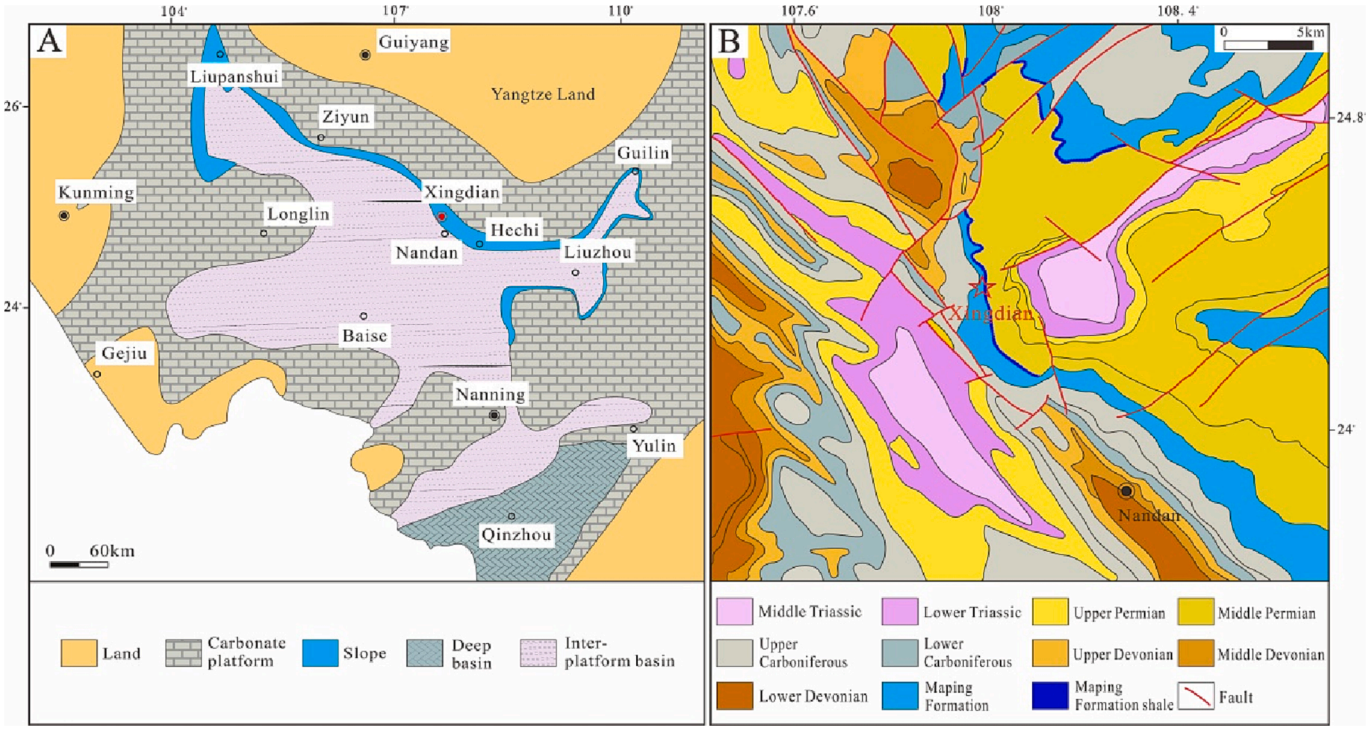

Fig. 1. (A) Sketch map showing the distribution of late Paleozoic sedimentary facies in the Youjiang Basin (modified from Qie and Wang, 2012). (B) Geological features of the Nandan area (modified from Guangxi Bureau of Geology and Mineral Exploration and Development, 1985).

deposits exceed the Li grade of brine (0.05 wt%) and pegmatite (0.28 wt %) deposits and are thus highly prospective (Kesler et al., 2012; Wen et al., 2020). Wen et al. (2020) regarded these deposits as carbonate-hosted clay-type Li resources and proposed their formation by the weathering and subsequent deposition of underlying basement carbonate rocks with no volcanism or associated hydrothermal and/or brine fluids being involved.

Lithium cannot be detected in fine-grained clay minerals by X-ray techniques due to the low-energy X-ray spectrum of Li, so sources and modes of occurrence of Li are unclear. Smectite has been suggested as the main Li-bearing mineral due to its strong adsorption capacity and the positive correlation between whole-rock Li and Mg contents (Cui et al., 2018; Wen et al., 2020; Zhao et al., 2022). Cookeite ($Al_2[(Si_3Al)O_{10}](OH)_2{\cdot}(Al_2Li)(OH)_6$), a Li-bearing chlorite, has been discovered in many bauxite-related Li-rich claystones including those in Pingguo, Guangxi (Ling et al., 2021), Yuxi, Yunan (Cui et al., 2022), and Henan (Song et al., 1987) provinces, and is considered a likely carrier of Li. Kaolinite has been considered another likely Li-bearing mineral due to its high Li content and the positive correlation between whole-rock Li and Si contents in Li-rich claystones (Zhang et al., 2022). Thus, the mode of occurrence of Li in carbonate-hosted clay-type Li resources remains unclear. The study of the genesis of various Li-rich minerals in sedimentary rocks is helpful to identify the origin of clay-type Li resources.

Here we focus on newly discovered Li-rich shales (~1000 ppm Li) in the Nandan area, Guangxi, SW China. Mineralogical and geochemical studies, and *in situ* analyses were undertaken on shale samples from a typical profile to identify Li-bearing minerals and elucidate the origin of the Li. Our results provide new insights into the behaviour of Li in near-surface environments and the genesis of clay-type Li resources.

2. Geological setting

The Nandan area is located in the northern Guangxi Province, SW China. It lies in the northern margin of the Youjiang Basin, which is a continental marginal basin formed by rifting on the basis of the South China Caledonian fold belt during the Late Palaeozoic (Fig. 1A; Jiang et al., 1987; Du et al., 2009; Wu et al., 2009; Qie and Wang, 2012; Liu et al., 2017; Wang et al., 2020). The evolution of the northern margin of the Youjiang Basin was controlled by the Hercynian syngenetic rifting and can be divided three stages: (1) intense rifting stage (early Carboniferous), (2) reduced rifting stage, and (3) stable rifting stage (late Carboniferous-early Permian) (Qie and Wang, 2012). During late Carboniferous-early Permian, the Youjiang Basin developed four types of sedimentary environments: carbonate platforms, slopes, inter-platform basins and deep-water basins (Fig. 1A; Qie and Wang, 2012). The lithology mainly comprises sandstone, carbonaceous shale, siliceous mudstone, siliceous rock, debris flow deposits, mudstone and dolomitic limestone (Shi et al., 2006; Qie and Wang, 2012). In the Nandan area, the exposed strata of Carboniferous-Lower Permian include (1) the Luzai Formation (Wangyou Formation, Muhua Formation, and Dawuba Formation), Baping Formation (Shangsi Formation and Dapu Formation), Nandan Formation (Huanglong Formation and Maping Formation), and Sidazhai Formaiton (Qixia Formation) (Fig. 2; Qie and Wang, 2012). The Li-rich black shale occurs at the top of the upper Carboniferous-lower Permian Maping Formation, which was deposited in the intermediate to deep-water slope/shelf setting along the northern part of the Nandan region, with a thickness of 282 to 920 m (Fig. 1A; Qie and Wang, 2012). The Li-rich shale displays conformable contacts with the underlying Maping Formation limestone and overlying lower Permian Qixia Formaiton limestone with thickness range from 0 to 80 m (Fig. 1B and 2). 49 shale samples were collected from the Xingdian section, northwest Nandan County. The section was systematically sampled throughout the stratigraphic succession (XD-H49 to XD-H1) (Fig. 3A). Shale samples are usually black or ash-black in color and have lamellar texture (Fig. 3B and C). Eight of these samples (XD-H1–H4 and XD-H32–H35) were weathered, usually yellow in color, and have an earthy texture (Fig. 3D).

3. Analytical methods

Forty-nine samples were collected from outcrops in the Xingdian section (Fig. 1B) for mineralogical and geochemical analyses. Whole-rock major- and trace-element analyses were undertaken by ALS

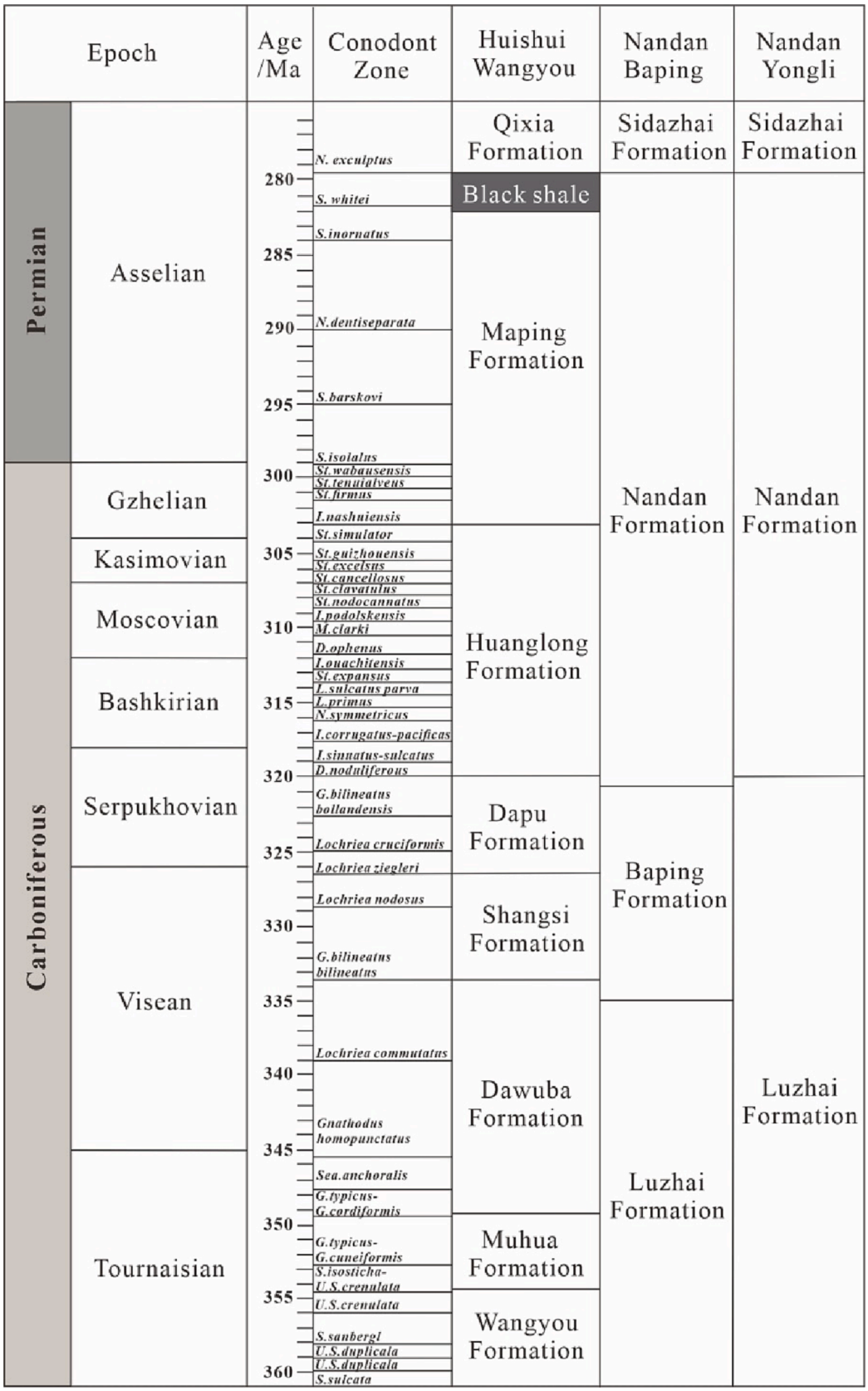

Fig. 2. Stratigraphic delineation of the Carboniferous-early Permian in the Nandan area (modified from Shi et al., 2006; Qie and Wang, 2012).

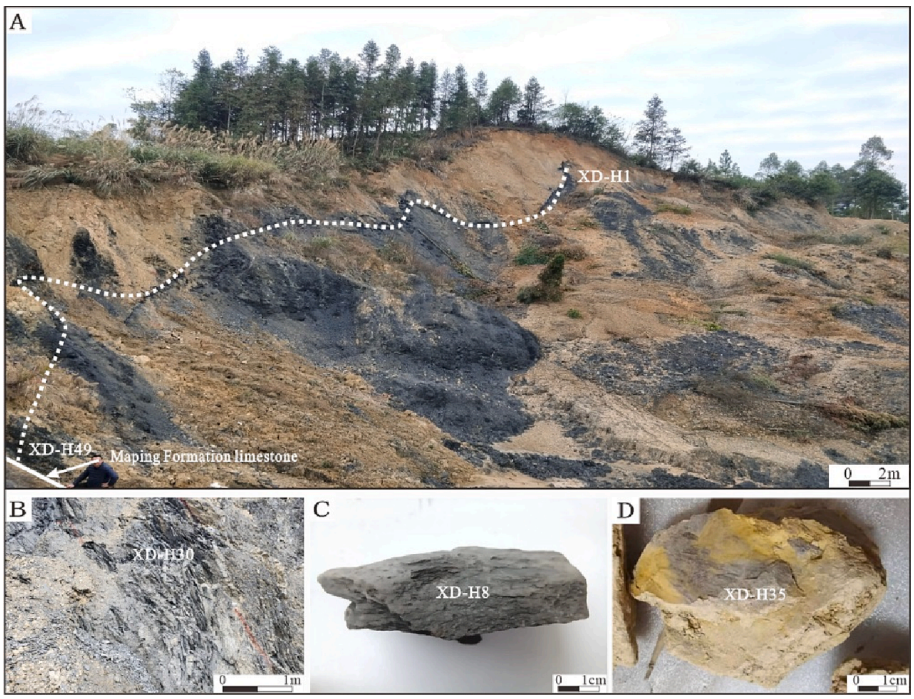

Fig. 3. Photographs of black shales in the Xingdian section, Nandan area. (A) Xingdian section; (B–C) Black shale samples; (D) Weathered shale sample.

Minerals-Guangzhou (Guangzhou, China). For major elements, samples were powdered to ~200 mesh in an agate mortar, fused with lithium metaborate or lithium borate, cooled and analysed by X-ray fluorescence spectroscopy (XRF), yielding relative standard deviation values of ≤10% (Table 1). Trace-element analyses were made by inductively coupled plasma–mass spectrometry (ICP–MS; PlasmaQuant Elite). Quality control involved analysis of national standards OU-6, AMH-1 and GBPG-1, which yielded reproducibility within ±10% for all trace elements (Table 1). Total organic carbon (TOC) analyses were conducted with an LECO Carbon/Sulfur Determinator at ALS Minerals-Guangzhou (Guangzhou, China), with analytical errors of less than ±5% (Table 1). Prior to the analyses, the sample powders were leached with 2.5 N HCl to remove inorganic carbon.

X-ray diffraction (XRD) analyses were undertaken at the Institute of Geochemistry, Chinese Academy of Sciences, Guiyang, China (IGCAS). Whole-rock XRD analyses were performed using a Panalytical Empyrean instrument equipped with a PIXcel3D detector, using Cu Kα1 radiation, 40 kV voltage, 40 mA beam current and the auto-flushing method for quantitative calculation. The details of the method are as follows (Ling et al., 2021): the software JADE was used to compare the main diffraction peaks (d value and intensity) with standard cards to determine the main mineral phase composition based on the best match; The semi-quantitative calculation uses the formula, $W_A = (I_A/R_A)/(I_A/R_A + I_B/R_B + I_C/R_C + \ldots) \times 100\%$, where W_A is the weight percentage of the mineral phase, I_A is the strongest peak, and R_A is the RIR value of the mineral phase to be measured, as shown in Table 2.

Representative samples were selected for thin-section analysis by dual-beam scanning electron microscopy–energy dispersive spectroscopy (SEM–EDS) (Scios, Thermo Fisher Scientific) at IGCAS. The typical sample XD-H8, with a whole-rock Li content of 1090 ppm, was cut to make a target foil (XDH-8) using a focused-ion-beam technique with SEM imaging, and this was used for time-of-flight secondary ion mass spectrometry (TOF–SIMS; IONTOF GmbH, Germany, TOF.SIMS 5–100) analysis at the National Central for Electron Spectroscopy, Tsinghua University, Beijing, China.

4. Results

4.1. Elemental geochemistry

The shale has Li contents of 95.7–1090 ppm; SiO_2 contents of 40.1–59.2 wt%; relatively low contents of CaO (0.19–11.4 wt%), Na_2O (0.75–1.32 wt%), K_2O (1.73–2.66 wt%), MgO (0.49–3.75 wt%) and TiO_2 (0.67–1.21 wt%); moderate contents of Al_2O_3 (13.1–23.9 wt%) and Fe_2O_3 (4.23–9.02 wt%); and chemical index of alteration (CIA) values of 35.4–83.1 (Table 1; Fig. 4). The black shale has a high TOC content of 0.71–1.53 wt% (average 1.03 wt%), which is much higher than the global average value (0.6 wt%) for fine-grained sediments formed under oxic conditions, indicating that the shale formed under anoxic depositional environment (Berner, 1982; Bennett and Canfield, 2020). In contrast, the weathered shales (XD-H1–H4 and XD-H32–H35) have a relatively low TOC content (0.17–0.52 wt%) due to the decomposition of organic matter during weathering.

4.2. Mineralogy

The mineral composition of the shale is dominated by illite and quartz, with small amounts of dolomite, chlorite, pyrite, calcite and halite (Table 2; Fig. 5). Illite is widely distributed and generally occurs as irregular flakes of size 1–100 μm (Fig. 6). Quartz and dolomite are granular in shape and typically of 10–50 μm in size. Pyrite commonly occurs as automorphic grains of 2–25 μm in size. Framboidal pyrite (Fig. 6I) indicates a reducing deposition environment. Chlorite occurs as small grains (<1 μm) in the matrix.

5. Discussion

5.1. Lithium occurrence

Shale whole-rock Li contents are either negatively or not correlated with Fe_2O_3, CaO, MgO, Na_2O and S contents (Fig. 7C–F, H), so dolomite, pyrite, calcite, chlorite and halite cannot be Li carriers. In contrast, the strong positive correlations between Li content and Al_2O_3, SiO_2 and K_2O contents and CIA values (Fig. 7A–B, G, I) indicate that illite ($K_{0.7}Al_2[(Si,$

Table 1
Major-element (wt.%) and Li (ppm) contents, and CIA values of shale samples from the Xingdian section, Nandan area, Guangxi, SW China.

Sample number	Lithology	Thickness (m)	SiO_2	Al_2O_3	Fe_2O_3	MgO	CaO	Na_2O	K_2O	TiO_2	S	TOC	CIA	Li (ppm)
XD-H1	Weathered shale	56.88	57.1	22.9	7.68	0.49	0.19	1.2	2.58	0.94	0.01	0.17	81.7	860
XD-H2	Weathered shale	56.03	57	23.1	7.65	0.52	0.28	0.97	2.54	1.01	0.01	0.2	82.6	990
XD-H3	Weathered shale	54.95	59.2	23	4.8	0.55	0.71	0.97	2.65	0.96	0.01	0.52	80	1020
XD-H4	Weathered shale	54.51	58.2	23.6	5.59	0.55	0.43	0.8	2.48	0.98	0.01	0.42	83.1	950
XD-H5	Black shale	54.31	46.7	18.9	7.51	1.75	5.84	0.95	2.39	0.98	1.84	1.24	56.1	550
XD-H6	Black shale	53.4	44.8	19	7.37	2.13	5.98	0.94	2.35	1.06	2.23	1.29	56	520
XD-H7	Black shale	51.71	44.8	18.2	7.95	2.34	6.14	0.9	2.19	1.01	1.42	0.93	54.8	590
XD-H8	Black shale	50.77	51	20.5	5.97	1.63	3.79	0.91	2.25	1.05	0.32	1.06	65.4	1090
XD-H9	Black shale	49.73	56.4	22.1	4.73	1.06	1.14	0.89	2.54	1.08	0.34	1.15	77.8	870
XD-H10	Black shale	48.56	47.1	17.8	7.55	1.96	6.02	0.75	1.79	0.9	2.01	1.13	55.8	570
XD-H11	Black shale	47.32	45.4	19	7.56	2.05	5.69	0.95	2.33	0.91	2.14	1.28	56.8	590
XD-H12	Black shale	45.41	51.7	20.8	6.47	1.52	3.03	0.88	2.3	1.06	0.48	1.01	68.7	710
XD-H13	Black shale	44.28	53.8	20.5	4.27	1.45	3.37	0.93	2.45	1.05	0.59	1.05	66.5	480
XD-H14	Black shale	43.07	49.6	20	5.15	1.81	5.19	1.04	2.19	1.11	0.85	1.07	59.7	490
XD-H15	Black shale	42.38	55.4	22.6	4.40	1.07	1.54	0.96	2.47	1.21	0.25	1.18	76.1	750
XD-H16	Black shale	41.09	54.5	21.3	5.42	1.28	2.32	1.12	2.52	1.14	0.35	1.07	70.7	560
XD-H17	Black shale	40.21	47.9	16.7	7.74	2.04	6.16	0.89	2.17	0.9	1.92	1.06	52.6	315
XD-H18	Black shale	38.62	43.1	17.4	8	2.37	7.44	1.07	2.29	1.02	1.98	1.13	49.5	379
XD-H19	Black shale	37.41	52.3	18.1	4.81	1.87	5.36	1.06	2.26	0.89	0.54	1.53	56.5	389
XD-H20	Black shale	36.89	50.8	18.6	5.09	1.99	5.61	1.1	2.35	0.89	0.46	1.27	56	355
XD-H21	Black shale	35	44.5	18.6	7.65	2.03	6.6	0.93	2.3	0.91	2.16	1.1	53.7	344
XD-H22	Black shale	33.27	47.6	17	7.68	2.01	6.09	1.07	2.31	0.87	2.10	1.01	52.5	273
XD-H23	Black shale	31.94	47.1	16.3	7.14	2.46	7.04	1.09	2.26	0.9	1.47	1.01	48.8	176
XD-H24	Black shale	31.14	46.4	17.1	6.79	2.27	7.26	0.96	2.18	0.98	1.57	1.04	49.9	270
XD-H25	Black shale	30.09	47.5	17	6.54	2.43	7.3	1.22	2.24	0.85	0.97	0.71	48.9	222
XD-H26	Black shale	28.58	47.9	17.5	6.47	2.22	6.56	1.1	2.25	0.93	1.35	0.75	52	244
XD-H27	Black shale	26.54	50.8	17.8	5.26	2.16	6.22	1.07	2.40	0.91	0.53	0.75	53.1	222
XD-H28	Black shale	24.19	46.8	16.7	7.58	2.36	6.49	0.96	2.42	0.92	1.95	1.05	51	174
XD-H29	Black shale	23.16	48.7	16.8	6.79	2.23	6.32	0.87	2.34	0.93	1.63	0.98	52	177
XD-H30	Black shale	22.11	49.3	23	4.45	1.41	4.02	1.06	2.66	1.15	1.22	1.05	65.8	369
XD-H31	Black shale	21.05	48.2	15.9	7.08	2.48	6.77	1	2.19	0.95	2.06	0.84	49.4	175
XD-H32	Weathered shale	20.18	53.8	24	7.86	0.62	0.5	1.32	2.99	0.91	0.01	0.24	79.2	480
XD-H33	Weathered shale	19.53	55.4	24.1	7.31	0.61	0.5	1.21	2.93	0.9	0.01	0.22	79.8	446
XD-H34	Weathered shale	19.14	56	23.9	7.27	0.6	0.54	1.22	2.95	0.91	0.01	0.23	79.4	360
XD-H35	Weathered shale	18.56	56.6	23.6	6.62	0.56	0.52	1.19	2.95	0.88	0.03	0.26	79.5	364
XD-H36	Black shale	17.62	49.5	17.5	7.5	1.87	5.02	1.06	2.41	1.03	2.31	0.94	56.5	239
XD-H37	Black shale	16.57	39.6	14	9.02	3.54	10.3	0.87	1.98	0.86	2.00	1.00	38.6	163.0
XD-H38	Black shale	15.85	45.9	15.2	6.67	3.03	8.77	0.88	2.29	0.67	0.55	0.89	43.3	147.5
XD-H39	Black shale	14.61	46.6	15.1	6.28	3.1	8.95	0.92	2.28	0.77	0.41	0.91	42.7	110.5
XD-H40	Black shale	12.3	46	14.6	6.25	3.1	9.16	0.91	2.20	0.78	0.45	0.87	41.4	115.5
XD-H41	Black shale	10.87	46.5	15.6	7.53	2.7	7.53	0.97	2.16	0.91	1.60	0.99	47	137
XD-H42	Black shale	9.56	40.1	13.2	8.49	3.75	11.4	0.82	1.73	0.72	1.05	0.88	35.4	153
XD-H43	Black shale	8.25	45.3	14.6	6.45	2.8	9.68	0.93	1.99	0.87	0.98	0.89	40.7	144.5
XD-H44	Black shale	6.49	42.4	13.1	7.7	3.58	11	0.81	1.93	0.71	0.50	0.88	35.8	95.7
XD-H45	Black shale	5.28	49.3	17.5	5.69	2.3	6.66	0.92	2.41	0.87	0.65	1.05	51.8	197.5
XD-H46	Black shale	3.73	46.9	16.4	6.43	2.74	7.77	0.93	2.3	0.95	0.68	0.96	47.4	226
XD-H47	Black shale	2.69	51.2	15.9	5.88	2.32	6.65	0.91	2.3	0.87	1.03	1	49.7	264
XD-H48	Black shale	1.76	49.3	18	5.76	2.22	6.05	0.93	2.45	0.91	1.23	1.03	54.2	323
XD-H49	Black shale	0.85	50.3	17.1	5.96	2.16	6.29	0.97	2.61	0.77	0.85	1.02	51.9	259

Notes: CIA = $Al_2O_3/(Al_2O_3 + CaO^* + Na_2O + K_2O) \times 100$, where CaO* can be estimated by assuming reasonable CaO/Na_2O ratios. If the CaO molar proportion is less than that of Na_2O, measured CaO can be used for CaO*; while CaO molar proportion is greater than that of Na_2O, CaO* it is assumed to be equivalent to Na_2O (McLennan, 1993; Shao and Yang, 2012).

$Al)_4O_{10}](OH)_2$) may be the Li carrier. The positive correlation between Li and illite contents, and negative or no correlation between Li and dolomite, chlorite, and quartz contents support this inference (Fig. 8A–D).

TOF–SIMS surface analyses indicate that the Li-rich phases are characterized by elevated Al, Si and K contents, a moderate Na content, and low Mg, Fe and Ti contents (Fig. 9), further indicating that illite is the main host mineral of Li, consistent with whole-rock analysis results. In most of the Li-rich deposits at McDermitt, Nevada, USA, Li-rich illite is regarded as the primary Li mineral (tainiolite, [$KLiMg_2Si_4O10F_2$]; Castor and Henry, 2020).

5.2. Origin of Li-rich illite

Illite in soils and sediments is generally of detrital origin, resulting from the weathering of mica, K-feldspar and plagioclase under cold and arid climatic conditions (Reichenbach and Rich, 1975; Singer, 1989; Meunier and Velde, 2004). It can also be formed from other minerals during burial diagenesis and hydrothermal alteration (Worden et al., 2020). The Li-rich shale of the present study does not contain volcanic detritus or associated alteration, precluding the possibility of alteration by hydrothermal fluid (Fig. 6). The high content of illite in the shale (average 48%) and its coarse-grained and near-random orientations indicate a detrital origin (Fig. 6; Ehrmann et al., 2005; Fesharaki et al., 2007). Therefore, we conclude that Li-rich illite in the Nandan area is of detrital origin and was formed during continental weathering.

5.3. Implications for clay-type Li resources

Volcanic clay-type deposits occur mainly in continental basins, with Li structurally bound in clays such as hectorite and jadarite (Meshram et al., 2014; Verly and Geo, 2014; Benson et al., 2017). The Li is derived mainly from the dissolution and leaching of adjacent Li-rich volcanic materials, and the mineral assemblage of ore is mainly K-feldspar,

Table 2
Mineral contents (%) of shale samples from the Xingdian section.

Sample	Quartz	Illite	Chlorite	Dolomite	Calcite	Pyrite	Halite
XD-H1	40.8	49.2	10				
XD-H2	31.6	58	10.4				
XD-H3	33	62	5.1				
XD-H4	30.1	61.3	8.6				
XD-H5	24.9	49.9	6.9	13.8	2.6	2	
XD-H6	23.5	53.4	8.5	12.8		1.8	
XD-H7	25.7	42.8	9.3	18.3		2.0	1.8
XD-H8	28.1	55.4	4.6	8.1		1.4	2.4
XD-H9	28	59.5	8.3	1.1		0.7	2.4
XD-H10	26.2	41.2	12.2	16.7	1.4	1.5	0.7
XD-H11	24.7	56.3	1.9	14.2		2.4	0.5
XD-H12	27.3	53.3	10.4	6.6		1.4	1.1
XD-H13	31.7	45.9	11.9	7.7		1.6	1.2
XD-H14	27	44.5	11.6	15.3		0.8	0.8
XD-H15	27.6	57.2	10.8	1.7		0.6	2.1
XD-H16	29.8	61	5.5	0.9		1.1	1.7
XD-H17	26.8	44.8	10.1	16.1		2.2	
XD-H18	24.2	48.5	6.3	18.9		2.2	
XD-H19	28.8	53.5	6.2	10.5		1	
XD-H20	28.8	51.8	6.3	12.2		0.9	
XD-H21	22.2	46.5	13.8	13.4	2.1	2.1	
XD-H22	27.1	44.7	9.5	16.2		2.4	
XD-H23	31.9	36.6	10.5	19.1		2.0	
XD-H24	25.7	46.8	10.3	13.6	2.0	1.6	
XD-H25	27.5	52	5.1	14.3		1.2	
XD-H26	27.3	51.7	4.6	15.3		1.1	
XD-H27	31.6	52.6	3.0	11.8		1	
XD-H28	30.9	40.2	6.5	20.4		2.1	
XD-H29	33.1	32	11.4	21.6		2.0	
XD-H30	20.8	56.3	13.4	7.2	1.4	0.9	
XD-H31	31.9	37.9	7.3	20.5	0.1	2.3	
XD-H32	28.1	64.0	6.6			1.3	
XD-H33	26.3	65.3	7.1			1.3	
XD-H34	25.5	67.8	5.1			1.6	
XD-H35	26.6	65.4	6.8			1.2	
XD-H36	37.8	51.3	7.4			3.6	
XD-H37	23.9	34.8	6.2	32.5		2.6	
XD-H38	30.9	34.0	5.3	28.4		1.3	
XD-H39	26.5	41.4	6.5	24.3		1.4	
XD-H40	31.3	30.2	6.3	31.2		1	
XD-H41	32.2	31.8	9.2	24.6		2.2	
XD-H42	27.6	28.6	4.0	36.1		3.7	
XD-H43	28.8	33.2	8.6	25	3	1.5	
XD-H44	29.2	33.3	4.3	31.6	0.1	1.5	
XD-H45	26.7	47.4	6.5	17.7	0.1	1.6	
XD-H46	31.2	38.3	4.5	24.8	0.2	1.1	
XD-H47	35.9	37.9	3.6	21.1		1.5	
XD-H48	31.2	44.1	7.5	15.6		1.6	
XD-H49	33.3	40.6	5.2	19.7		1.2	

quartz, calcite, albite, illite, hectorite and/or jadarite (Benson et al., 2017; Castor and Henry, 2020). For example, the McDermitt/King Valley Li deposit (USA) comprises layers of hectorite in a sequence of sedimentary and tuffaceous rocks. The Li was leached from rhyolitic volcanic rocks and tephra by meteoric and hydrothermal fluids, and is structurally bound in hectorite that formed in tephra-rich sediments in a caldera basin (Benson et al., 2017). In carbonate-hosted clay-type resources, Li is mainly adsorbed to or structurally bound in clays such as smectite, cookeite and kaolinite (Wen et al., 2020; Ling et al., 2021; Zhang et al., 2022). The Li-rich claystone is generally associated with karst bauxite deposits (i.e., Al-rich sedimentary rocks deposited on a carbonate unconformity) that formed in continental or coastal basins (e.g., Song et al., 1987; Yang et al., 2019a; Yang et al., 2019b; Ling et al., 2021). The mineral assemblage of Li-rich claystone is mainly clay (kaolinite, illite, chlorite and smectite) and Al-rich (diaspore and boehmite) minerals, along with accessory minerals (e.g., zircon, rutile and anatase) and Fe-bearing phases (e.g., pyrite, hematite and goethite) (Wang et al., 2013; Wen et al., 2020; Cui et al., 2022; Zhang et al., 2022). The deposition environment of carbonate-hosted clay-type Li resources is considered to be formed under fresh- or brackish-water conditions (Wen et al., 2020; Zhao et al., 2022).

The Nandan shale has different geological features (i.e., mineral assemblages, Li and fluid sources, and depositional environments) to volcanic clay type and carbonate-hosted clay type Li deposits, indicating it is a new type of Li-rich sedimentary rock. As it was formed in an intermediate to deep-water slope setting, our results indicate that Li-rich sedimentary rocks form not only in crater basins and continental or coastal basins, but also in the marine environment.

6. Conclusions

Black shale at the top of the upper Carboniferous-lower Permian Maping Formation in the Nandan area of northern Guangxi is rich in Li (~1000 ppm). Whole-rock Li contents are positively correlated with K_2O and illite contents, indicating that illite ($K_{0.7}Al_2[(Si,Al)_4O_{10}](OH)_2$) could be the Li carrier. This possibility is supported by TOF–SIMS analyses that show the Li-rich mineral is characterized by high Al, Si and K contents. Mineralogical studies indicate that the Li-rich illite is of detrital origin and was formed during continental weathering. The Nandan shale has different geological features (e.g., mineral

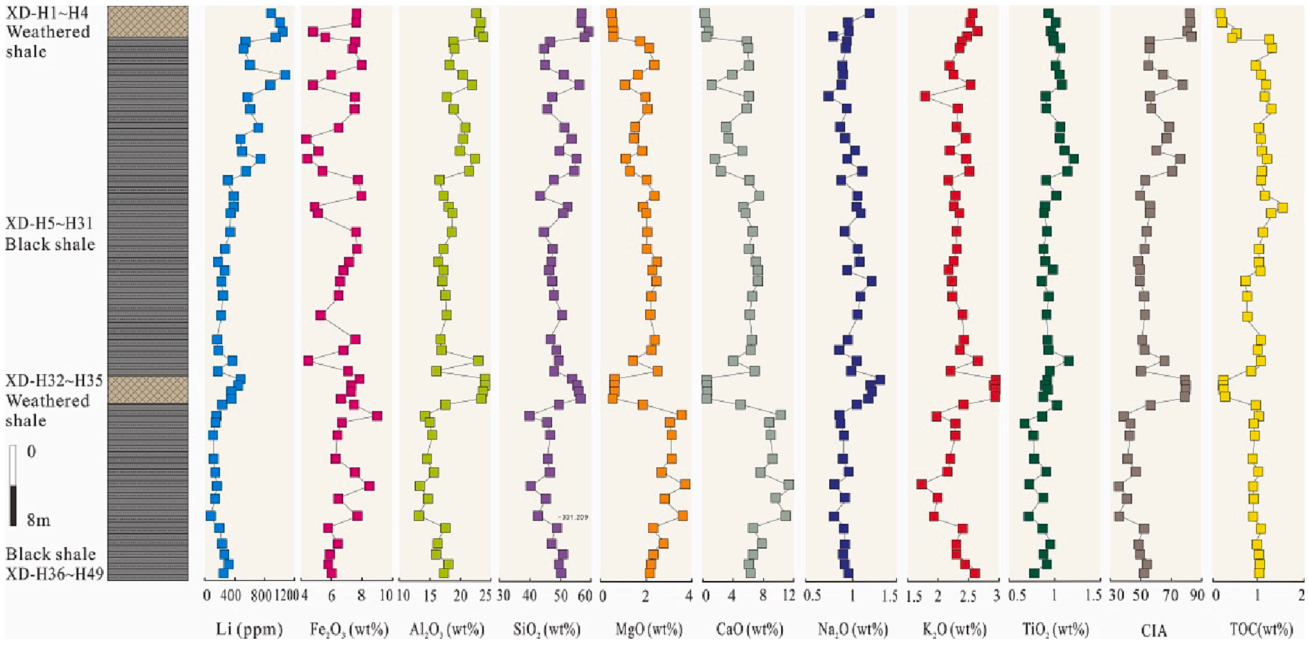

Fig. 4. Concentrations of selected elements and CIA values for the Xingdian section samples.

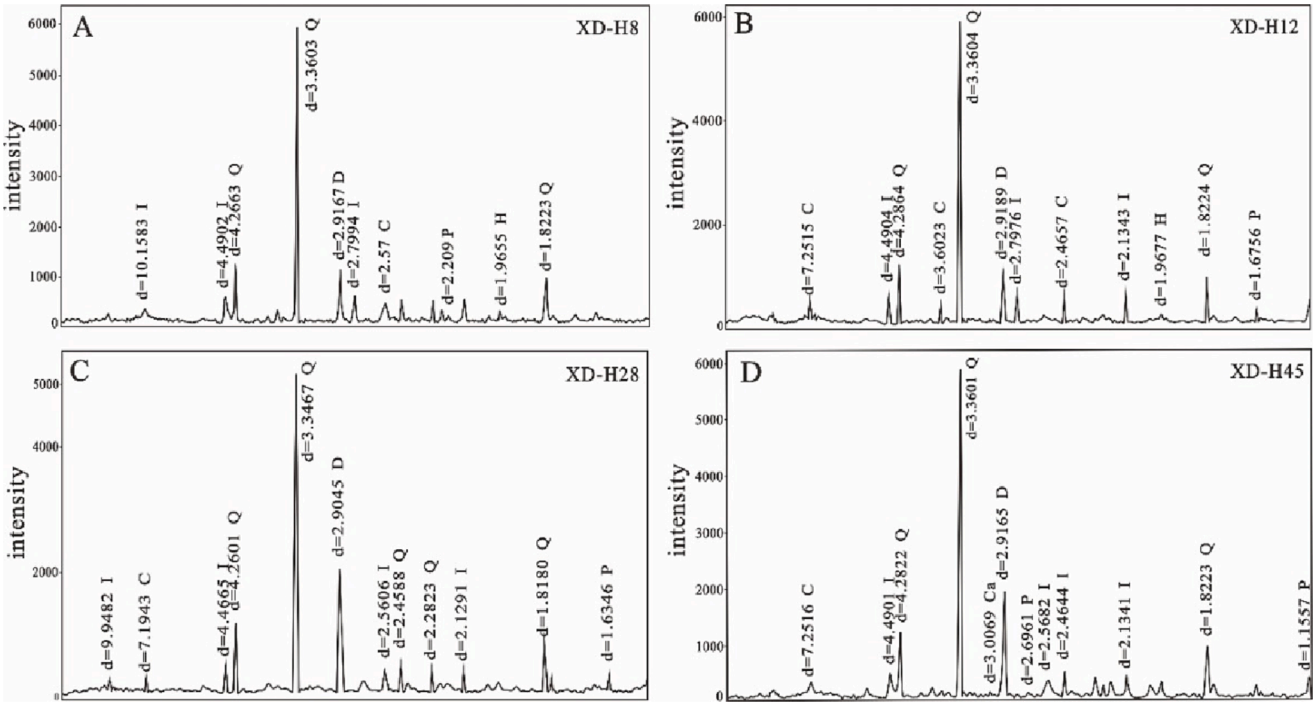

Fig. 5. XRD patterns of selected samples from the Xingdian section. Q, quartz; I, illite; D, dolomite; C, chlorite; P, pyrite; Ca, calcite; H, halite.

assemblages, Li and fluid sources, and depositional environment) to those of volcanic and carbonate-hosted clay-type Li resources, indicating that it represents a new type of Li-rich sedimentary rock. The widespread occurrence of framboidal pyrite and high TOC content in the shale suggests that the Li-rich shale was formed under anoxic depositional conditions. Our findings may provide additional reference material for study of the genesis of clay-type resources and provide new insights into the mechanisms of Li enrichment in surface environments.

Declaration of Competing Interest

The authors declare that they have no known competing financial interests or personal relationships that could have appeared to influence the work reported in this paper.

Data availability

No data was used for the research described in the article.

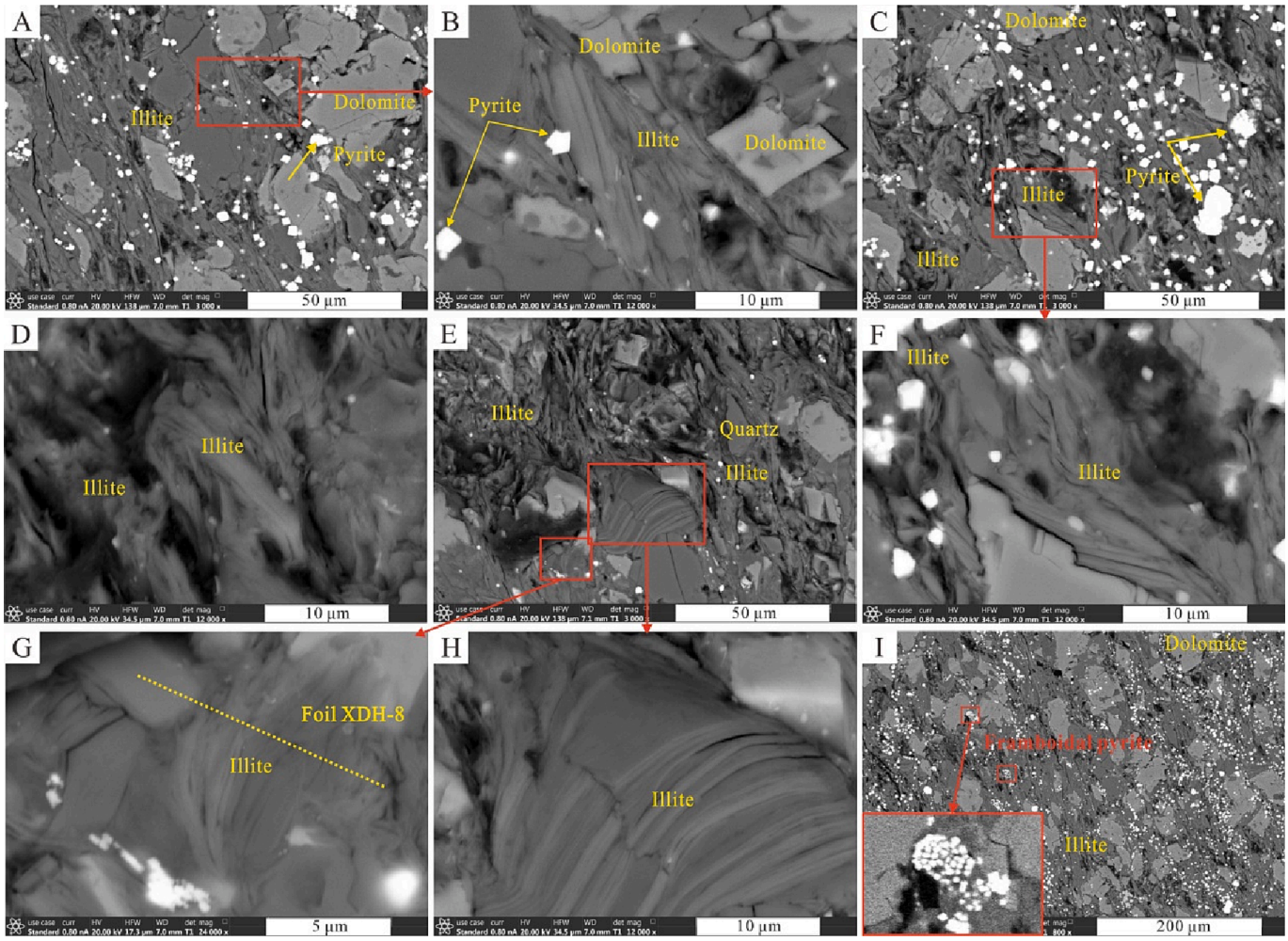

Fig. 6. SEM backscattered-electron images of Li-rich shale from the Maping Formation. (A–C) Coexisting lamellar illite, coarse-grained dolomite and fine-grained pyrite; (D) lamellar illite; (E) coexisting quartz and illite; (F) lamellar illite; (G) sampling site of foil XDH-8; (H) lamellar illite; and (I) coexisting illite, dolomite and framboidal pyrite.

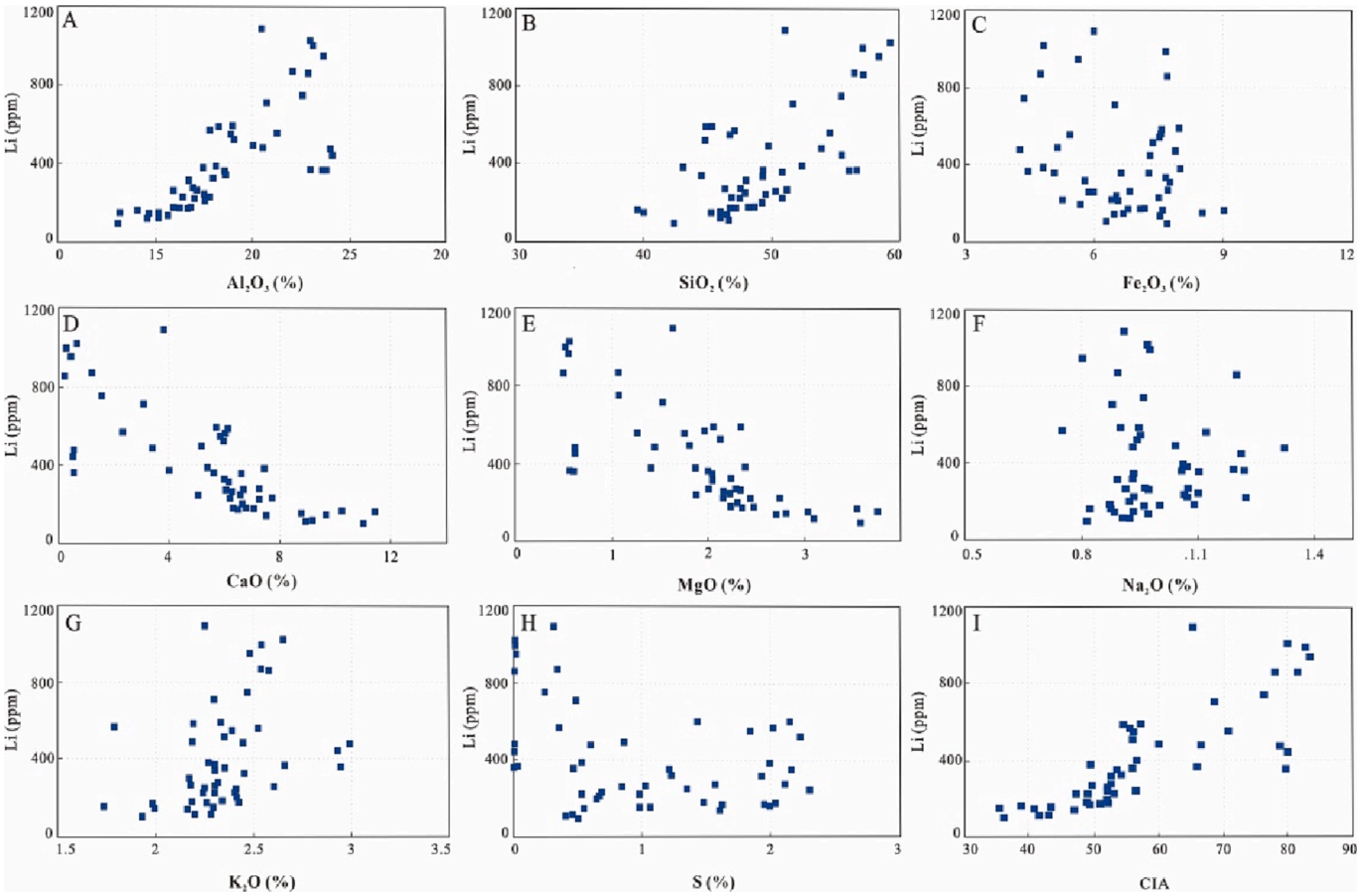

Fig. 7. Bivariate plots of Li content vs (A) Al_2O_3, (B) SiO_2, (C) Fe_2O_3, (D) CaO, (E) MgO, (F) Na_2O, (G) K_2O and (H) S contents, and (I) CIA values.

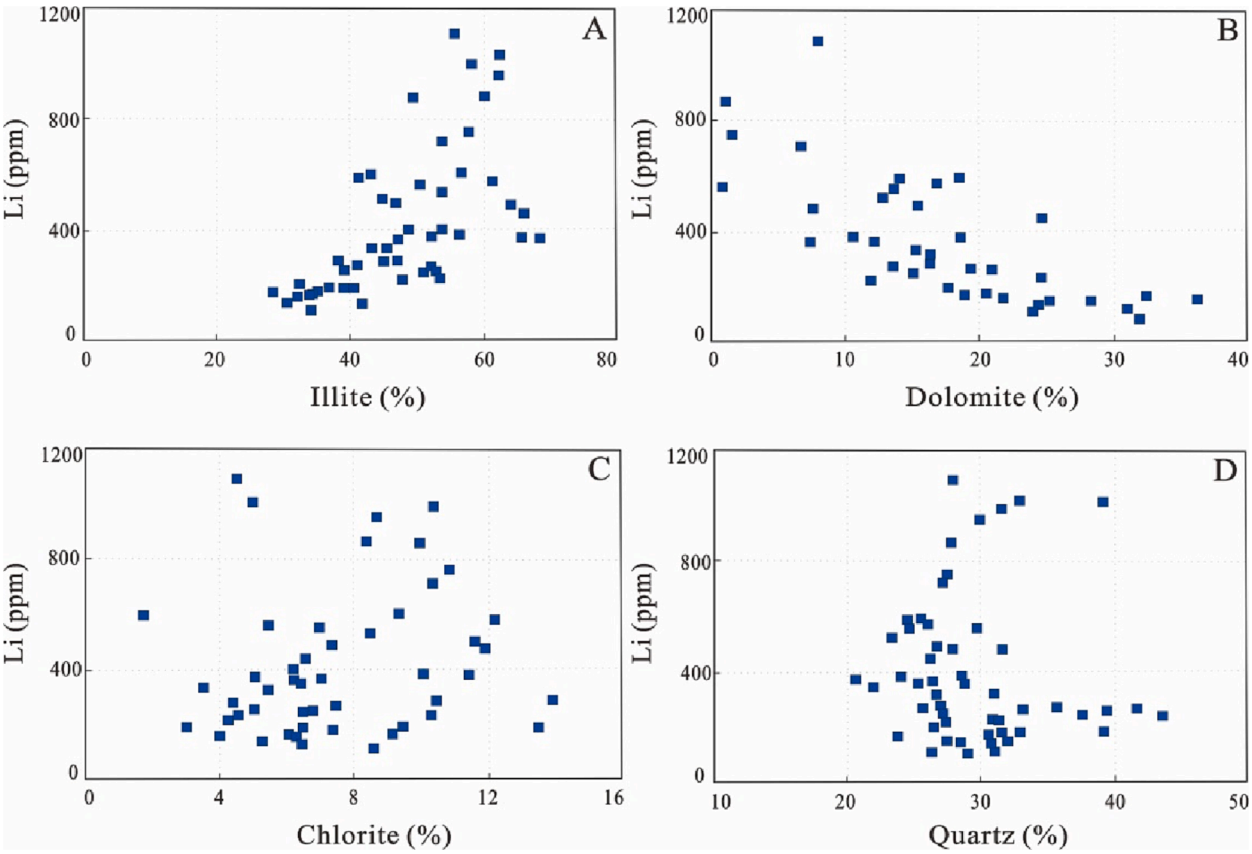

Fig. 8. Bivariate plots of Li content vs (A) illite, (B) dolomite, (C) chlorite, (D) quartz, (E) pyrite and (F) halite contents.

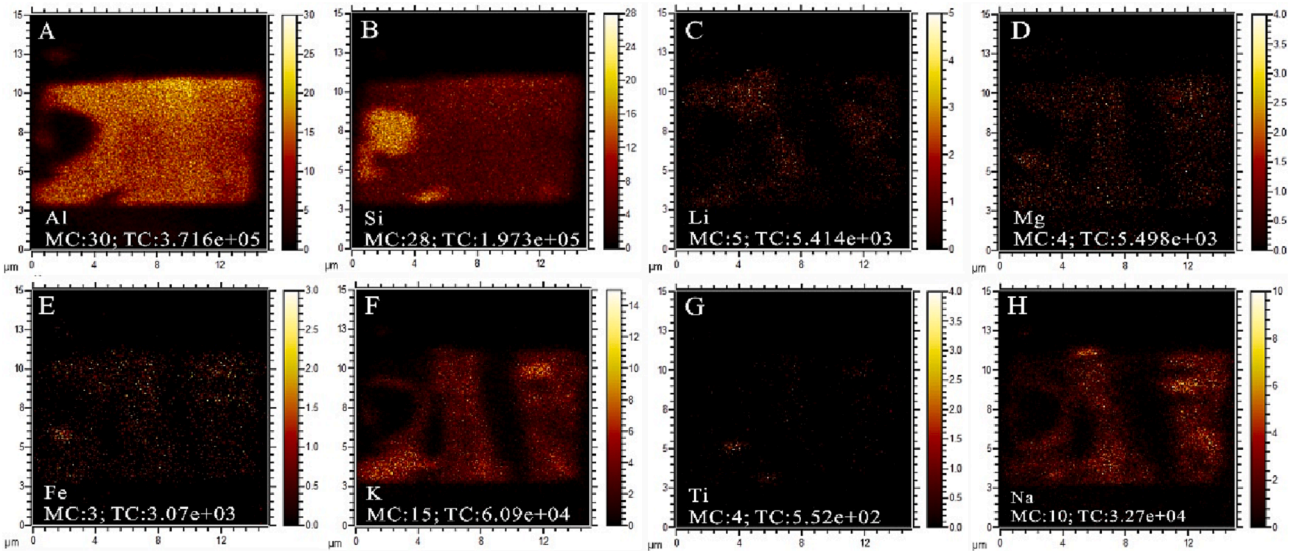

Fig. 9. TOF–SIMS images of foil XDH-8 showing the microscale distribution of selected elements.

Acknowledgements

This work was supported by the National Natural Science Foundation of China (grants 92162214, 92062107), the Key R&D Program of Yunan Province (grant 202103AQ100003), the Qian Sci & Tec Supporting Plan (ZK[2021] key program 046), the Key Research Program of the Chinese Academy of Sciences (grant ZDRW-ZS-2020-4-1), and the Key Research Program of the Institute of Geology & Geophysics, CAS (Grant IGGCAS-201902).

References

Bennett, W.W., Canfield, D.E., 2020. Redox-sensitive trace metals as paleoredox proxies: A review and analysis of data from modern sediments. Earth-Sci. Rev. 204, 103175.
Benson, T.R., Coble, M.A., Rytuba, J.J., Mahood, G.A., 2017. Lithium enrichment in intracontinental rhyolite magmas leads to Li deposits in caldera basins. Nat. Commun. 8, 270.
Berner, R.A., 1982. Burial of organic carbon and pyrite sulfur in the modern ocean: its geochemical and environmental significance. Am. J. Sci. 282, 451–473.
Bowell, R.J., Lagos, L., de los Hoyos, C.R., Declercq, J., 2020. Classification and characteristics of natural lithium resources. Elements 16, 259–264.
Bradley, D.C., McCauley, A.D., Stillings, L.L., 2017. Mineral-Deposit Model for Lithium-Cesium-Tantalum Pegmatites. US Geological Survey.
Castor, S.B., Henry, C.D., 2020. Lithium-rich claystone in the McDermitt Caldera, Nevada, USA: geologic, mineralogical, and geochemical characteristics and possible origin. Minerals 10, 68.
Chen, P., Chai, D.H., 1997. Sedimentary Geochemistry of Carboniferous Bauxite Deposits in Massif. Shanxi Science and Technology Press, Taiyuan.
Cui, Y., Luo, C., Xu, L., Zhang, H., Deng, M., Gu, H., Meng, Y., Qin, C., Wen, H., 2018. Weathering origin and enrichment of lithium in clay rocks of the Jiujialu Formation, Central Guizhou Province, Southwest China. Bull. Mineral. Petrol. Geochem. 37 (4), 696–704 in Chinese with English abstract.
Cui, Y., Wen, H., Yu, W., Luo, C., Du, S., Ling, K., Xu, F., Yang, J., 2022. Study on the occurrence state and enrichment mechanism of lithium in lithium-rich clay rock series of the Daoshitou Formation of Lower Permian in Central Yunnan. Acta Petrol. Sin. 38 (7), 2080–2094.
Du, Y.S., Huang, H.W., Huang, Z.Q., Xu, Y.J., Yang, J.H., Huang, H., 2009. Basin translation from Late Palaeozoic to Triassic of Youjiang Basin and its tectonic significance. Geol. Sci. Technol. Inf. 28 (6), 10–15 in Chinese with English abstract.
Ehrmann, W., Setti, M., Marinoni, L., 2005. Clay minerals in Cenozoic sediments off Cape Roberts (McMurdo Sound, Antarctica) reveal palaeoclimatic history. Palaeoecology 229, 187–211.
Fesharaki, O., García-Romero, E., Cuevas-González, J., López-Martínez, N., 2007. Clay mineral genesis and chemical evolution in the Miocene sediments of Somosaguas, Madrid Basin, Spain. Clay Miner. 42, 187–201.
Glanzman, R.K., Mccarthy, J.H., Rytuba, J.J., 1978. Lithium in the McDermitt caldera, Nevada and Oregon. Energy 3, 347–353.
Jiang, N.Y., Zhou, Z.R., Huang, Z.X., 1987. Deep-water carbonate debris flow and its geological significance in the upper section of the Maping Formation, Liuzhai, Nandan, Guangxi. J. Stratigr. 11 (04), 286–289.
Kesler, S.E., Gruber, P.W., Medina, P.A., Keoleian, G.A., Everson, M.P., Wallington, T.J., 2012. Global lithium resources: Relative importance of pegmatite, brine and other deposits. Ore Geol. Rev. 48, 55–69.
Ling, K., Tang, H., Zhang, Z., Wen, H., 2020. Host minerals of Li-Ga-V-rare earth elements in Carboniferous karstic bauxites in southwest China. Ore. Geol. Rev. 119, 103325.
Ling, K., Wen, H., Zhang, Q., Luo, C., Gu, H., Du, S., Yu, W., 2021. Super-enrichment of lithium and niobium in the upper Permian Heshan Formation in Pingguo, Guangxi, China. Sci. China Earth Sci. 64 (5), 753–772.
Liu, X., Wang, Q., Zhang, Q., Yang, S., Liang, Y., Zhang, Y., Li, Y., Guan, T., 2017. Genesis of the Permian karstic Pingguo bauxite deposit, western Guangxi, China. Mineralium Deposita 52, 1031–1048.
McLennan, S.M., 1993. Weathering and global denudation. J. Geol. 101, 295–303.
Meshram, P., Pandey, B.D., Mankhand, T.R., 2014. Extraction of lithium from primary and secondary sources by pre-treatment, leaching and separation: a comprehensive review. Hydrometallurgy 150, 192–208.
Meunier, A., Velde, B., 2004. Illite: Origin, Evolution and Metamorphism. Springer, New York.
Qie, W.K., Wang, X.D., 2012. Carboniferous-Early Permian deep-water succession in northern margin of the Dian-Qian-Gui Basin and its sedimentary evolution. Chin. J. Geol. 47 (4), 1071–1084 in Chinese with English abstract.
Reichenbach, H.G., Rich, C.I., 1975. Fine-grained micas in soils. In Geiseking J E (eds.) Soil components, Vol. 2, Inorganic components. New-York: Springer-Verlag, 59–95.
Rosales, G.D., Resentera, A.C.J., Gonzalez, J.A., Wuilloud, R.G., Rodriguez, M.H., 2019. Efficient extraction of lithium from β-spodumene by direct roasting with NaF and leaching. Chem. Eng. Res. Des. 150, 320–326.
Shao, J.Q., Yang, S.Y., 2012. Does chemical index of alteration (CIA) reflect silicate weathering and monsoonal climate in the Changjiang River basin? Chin. Sci. Bull. 57, 1178–1187.
Shen, L.P., Song, Y.H., Peng, Z.R., Guo, K.Z., 1986. Discovery and preliminary study of Li-chloritein claystone from acertain location of Henan province. Acta Mineral. Sin. 6, 86–91 in Chinese with English abstract.
Shi, X.Y., Hou, Y.A., Shuai, K.Y., 2006. Late Paleozoic deep-water stratigraphic succession in central Youjiang Basin: constraints on basin evolution. Earth Sci. Front. 13 (6), 153–170.
Singer, A., 1989. Illite in the hot-aridic soil environment. Soil Sci. 147, 126–133.
Song, Y.H., Shen, L.P., Zhang, N.X., Peng, Z.R., Guo, K.Z., 1987. A preliminary study on clay minerals and REE and Li in clay ore (rocks) in Henan Province. Sci. China Ser. B 59, 324–326.
Stanley, C.J., Jones, G.C., Rumsey, M.S., Blake, C., Roberts, A.C., Stirling, J.A.R., Carpenter, G.J.C., Whitfield, P.S., Grice, J.D., Lepage, Y., 2007. Jadarite, $LiNaSiB_3O_7(OH)$, a new mineral species from the Jadar Basin, Serbia. Eur. J. Mineral. 19, 575–580.
Stojadinovic, U., Matenco, L., Andriessen, P., Toljić, M., Rundić, L., Ducea, M.N., 2017. Structure and provenance of Late Cretaceous-Miocene sediments located near the NE Dinarides margin: Interferences from kinematics of orogenic building and subsequent extensional collapse. Tectonophysics 710, 184–204.
Tinto, R., 2017. Notice to ASX, Increase to Jadar Project Mineral Resources 2 March 2017, 22p.
Wang, D.H., Li, P.G., Qu, W.J., Yin, L.J., Zhao, Z., Lei, Z.Y., Wen, S.F., 2013. Discovery and preliminary study of the high tungsten and lithium contents in the Dazhuyuan bauxite deposit, Guizhou, China. Sci. China Earth Sci. 56, 145–152.
Wang, W.F., Qin, Y., Liu, J.T., Li, J., Yuan, L., 2012. Mineral microspherules in Chinese coal and their geological and environmental significance. Int. J. Coal Geol. 94, 111–122.
Wang, Q., Yang, L., Xu, X., Santosh, M., Wang, Y., Wang, T., Chen, F., Wang, R., Gao, L., Liu, X., Yang, S., Zeng, Y., Chen, J., Zhang, Q., Deng, J., 2020. Multi-stage tectonics and metallogeny associated with Phanerozoic evolution of the South China Block: A holistic perspective from the Youjiang Basin. Earth-Sci. Revi. 211, 103405.

Wen, H., Luo, C., Du, S., Yu, W., Gu, H., Ling, K., Cui, Y., Li, Y., Yang, J., 2020. Carbonate-hosted clay-type lithium deposit and its prospecting significance. Chin. Sci. Bull. 65, 53–59.

Worden, R.H., Griffiths, J., Wooldridge, L.J., Utley, J.E.P., Lawan, A.Y., Muhammed, D. D., Simon, N., Armitage, P.J., 2020. Chlorite in sandstones. Earth Sci. Rev. 204, 10310.

Wu, G., Yao, G., Xu, Z., Guo, Q., Chen, Z., 2009. Structural patterns and origin of tectonic reformation in guizhong depression. Mar. Origin Petrol. Geol. 14 (01), 33–40 in Chinese with English abstract.

Yang, M.J., Liang, X.L., Ma, L.Y., Hang, J., He, H.P., Zhu, J.X., 2019a. Adsorption of REEs on kaolinite and halloysite: A link to the REE distribution on clays in the weathering crust of granite. Chem. Geol. 525, 210–217.

Yang, S., Wang, Q., Deng, J., Wang, Y., Kang, W., Liu, X., Li, Z., 2019b. Genesis of karst bauxite-bearing sequences in Baofeng, Henan (China), and the distribution of critical metals. Ore Geol. Rev. 115, 103161.

Yu, Y., Lin, L.B., Gao, J., 2016. Formation mechanisms and sequence response of authigenic grain-coating chlorite: evidence from the Upper Triassic Xujiahe Formation in the southern Sichuan Basin, China. Pet. Sci. 13, 657–668.

Zhang, J.Y., Wang, Q.F., Liu, X.F., Zhou, G.F., Xu, H.P., Zhu, Y.G., 2022. Provenance and ore-forming process of Permian lithium-rich bauxite in central Yunnan, SW China. Ore Geol. Rev. 145, 104862.

Zhao, Y., Ma, W., Yang, Y., Cui, Y., Xu, L., Luo, C., Wen, H., 2022. Experimental study on the adsorption of Li^{+} by clay minerals — implications for the mineralization of clay-type lithium deposit. Acta Mineral. Sin. 42 (2), 141–153 in Chinese with English abstract.